metals

MDPI

Article

Enhanced Hydrogen-Storage Properties of MgH_2 Catalyzed via a Cerium Doped TiCrV BCC Alloy

Houqun Xiao [1,2], Xiaoxuan Zhang [1,2], Chenyu Li [2], Yuehai Li [1], Chuanming Ma [2,*], Ruixiang Wang [1], Luocai Yi [2] and Qingjun Chen [1,2,*]

[1] Faculty of Materials Metallurgy and Chemistry, Jiangxi University of Science and Technology, Ganzhou 341000, China; hqxiao21@gia.cas.cn (H.X.)
[2] Key Laboratory of Rare Earths, Chinese Academy of Sciences, Jiangxi Institute of Rare Earths, Ganjiang Innovation Academy, Chinese Academy of Sciences, Ganzhou 341000, China
* Correspondence: cmma@gia.cas.cn (C.M.); qjchen@gia.cas.cn (Q.C.)

Abstract: In this work, Ce-doped $Ti_6Cr_{14}V_{80}$ BCC hydrogen-storage alloys have been synthesized as catalysts to enhance the hydrogen-storage performance of MgH_2 based on its room-temperature activation features and excellent durability. The $Ti_6Cr_{14}V_{80}Ce_1$ alloy was pre-ball milled under a hydrogen atmosphere into a $Ti_6Cr_{14}V_{80}Ce_1H_x$ hydride. Different amounts of the $Ti_6Cr_{14}V_{80}Ce_1H_x$ hydride were incorporated into MgH_2 by ball milling to obtain the MgH_2 + y wt%$Ti_6Cr_{14}V_{80}Ce_1H_x$ (y = 0, 3, 5, 10, 15) nano-composites. With an optimization doping of 10 wt%$Ti_6Cr_{14}V_{80}Ce_1H_x$, the initial dehydrogenated temperature was decreased to 160 °C. Moreover, the composite can rapidly release 6.73 wt% H_2 within 8 min at 230 °C. Also, it can absorb 2.0 wt% H_2 within 1 h even at room temperature and uptake 4.86 wt% H_2 within 10 s at 125 °C. In addition, the apparent dehydrogenated activation energy of the MgH_2 + 10 wt%$Ti_6Cr_{14}V_{80}Ce_1H_x$ composite was calculated to be 62.62 kJ mol^{-1} fitted by the JMAK model. The capacity retention was kept as 84% after 100 cycles at 300 °C. The ball milled $Ti_6Cr_{14}V_{80}Ce_1H_x$ transformed from the initial FCC phase structure into a BCC phase after complete dehydrogenation and back into an FCC phase when fullly hydrogenated. A catalyst mechanism analysis revealed that the 'autocatalytic effect' originating in $Ti_6Cr_{14}V_{80}Ce_1H_x$ plays a crucial role in boosting the de-/hydrogenation properties of MgH_2. This work provides meaningful insights into rational designs of nano-compositing with different hydrogen-storage alloy catalyzed MgH_2.

Keywords: $Ti_6Cr_{14}V_{80}Ce_1H_x$; MgH_2; nano-compositing; hydrogen storage; catalyst mechanism

Citation: Xiao, H.; Zhang, X.; Li, C.; Li, Y.; Ma, C.; Wang, R.; Yi, L.; Chen, Q. Enhanced Hydrogen-Storage Properties of MgH_2 Catalyzed via a Cerium Doped TiCrV BCC Alloy. *Metals* **2024**, *14*, 572. https://doi.org/10.3390/met14050572

Academic Editor: Babak Shalchi Amirkhiz

Received: 14 April 2024
Revised: 9 May 2024
Accepted: 9 May 2024
Published: 13 May 2024

Correction Statement: This article has been republished with a minor change. The change does not affect the scientific content of the article and further details are available within the backmatter of the website version of this article.

1. Introduction

The current prevailing energy sources, fossil fuels, have brought severe challenges for human survival such as pollution and irreversible carbon emission [1,2]. Excessive reliance on unsustainable fossil fuels is undesirable and the crisis of energy exhaustion is gradually approaching. Exploring alternative energy sources to fossil fuels has been a basic consensus of all the countries. Consequently, it is undoubted that developing alternative environmentally cleaner fuels are crucial for a sustainable future [3]. Hydrogen, as a clean energy carrier, has drawn sustained attention as an alternative to fossil fuels owing to its pollution-free and high calorific value of combustion. It is believed that hydrogen acts as the most promising non-fossil fuel and will play a crucial role in reducing the release of greenhouse gases and realizing zero carbon emissions. However, one major concern for widespread implementation of hydrogen is lack of safe, convenient and economic hydrogen-storage methods [4,5]. Currently, hydrogen is often stored in the gas by compression in pressure vessels or in liquid form at below 20 K in cryogenic tanks [6,7]. Even though these two types of hydrogen storage have been matured and commercialized, its use is still challenging for various applications due to high energy demands, expensive tank cost

and intrinsic safety risks [8,9]. Therefore, it is imperative to develop safe, cost-effective, reliable hydrogen-storage techniques for large-scale application. Thus, the solid-state storage technique has attracted increasing attention; it possesses the extra advantages of being lightweight, high-capacity, reliable, easy to operate and cost-effective compared to other techniques [10,11]. It is worth pointing out that metal hydrides are widely researched and developed because they show high hydrogen-storage densities, excellent sorption reversibility and fast kinetic performance [12–14].

Metal hydrides usually form interstitial hydrides in which atomic hydrogen occupies interstitial voids in the crystal, which typically includes $LaNi_5$, AB, AB_2 or V-based body-centered cubic (BCC) alloys [15–18]. Though the V-based BCC alloys have maximum theoretical hydrogen-storage capacity~3.8 wt% among them, they face the problem of difficult activation and keeping residual hydrogen in the alloys [19]. Furthermore, it has been verified that the content of vanadium plays a crucial role in the cyclic stability of the typical Ti-Cr-V BCC-type hydrogen-storage alloy [20]. It has been reported that the Ti-Cr-V alloy with the V content exceeding 75 at% demonstrated excellent durability [21]. The higher the V content they have, the stronger the toughness the alloy possesses and the more difficult it is to break. One of the typical shortcomings of the Ti-Cr-V alloys is that it is challenging to activate under ambient conditions. Nevertheless, doping with few light rare earth lanthanum (La) or cerium (Ce) could make the V-based BCC alloy easier to activate and cause faster absorption of hydrogen [22,23]. It has been reported that La/Ce elements have strong affinity with oxygen. Liu et al. [24] found that a small amount of 0.4% Ce doped into $Ti_{32}Cr_{46}V_{22}$ alloy can activate it and cause it to absorb hydrogen at room temperature. Xue et al. [23] prepared $TiCr_3V_{16}Ce_x$ alloys by doping different amount of Ce and revealed the hydrogen-storage mechanism of the alloy.

Magnesium hydride was considered as a promising solid hydrogen-storage medium on account of its outstanding reversible storage capacity of 7.6 wt% and the abundance of magnesium resources on earth. However, sluggish de-/absorption kinetics and stable thermodynamic characteristics cause it to have high operation temperature and inferior sorption rate [25]. To this end, massive strategies have been carried out to tailor its thermodynamics and kinetics, combining the alloying, nanosizing, catalyzing and compositing with other hydrides, and so on [26–29]. Recently, by adding the AB_2 or BCC hydrogen-storage alloys, with excellent hydrogen de-/absorption features at room temperature, as catalytic additives into MgH_2 to fabricate nano-compounds, one can regulate the thermodynamics and kinetics of MgH_2 during the de-/hydrogenation process. Yu et al. [30] found that the ball milled MgH_2-20 wt%$Ti_{0.4}Cr_{0.15}Mn_{0.15}V_{0.3}$ composite could absorb 90% of its initial hydrogen capacity within 1.5 h at below 100 °C. Lu et al. [31] adopt the prepared $Ti_{0.9}Zr_{0.1}Mn_{1.5}V_{0.3}$ (AB_2 Laves phase) alloy accompanied with CNTs as aid agent to modify the hydrogen-storage properties of MgH_2. The ball milled MgH_2 + 10 wt%$Ti_{0.9}Zr_{0.1}Mn_{1.5}V_{0.3}$ + 1wt% CNTs composite can uptake H_2 at room temperature and release 6.1 wt% in 5 min at 300 °C. It was verified both experimentally and theoretically that local destabilization of Mg-H bonds was induced by MgH_2/alloy interfaces. Zhang et al. [32] also synthesized the MgH_2-20 wt% $Ti_{0.35}Cr_{0.45}V_{0.2}$ composite by reactive ball milling under 5.0 MPa H_2, which revealed nanocrystalline β-MgH_2, γ-MgH_2 and Ti-Cr-$V_{0.2}H_y$ ($1.91 < y < 2.01$) phases were generated in the composites and the favorable synergetic desorption effect from three phases probably results in remarkable dehydrogenation kinetics performance of the Mg/MgH_2 system. However, different particle sizes existed in the current alloy-catalyzed MgH_2 systems. The diversity was attributed to the large grain size of the alloy created by the difficult activation. In particular, the alloys were often activated after high-temperature processing and then added into MgH_2 according to the previous Ti-Cr-V alloy-catalyzed MgH_2 [33,34]. Here, we adopt Ce-doped $Ti_6Cr_{14}V_{80}$ BCC hydrogen-storage alloys via pre-ball milled under hydrogen pressure to generate the $Ti_6Cr_{14}V_{80}Ce_1H_x$ hydride; these were then added into MgH_2 to build the compounded material. The Ce-doped $Ti_6Cr_{14}V_{80}$ alloy can easily absorb hydrogen under mild conditions. Pre-ball milling in a hydrogen atmosphere can make it more uniform and cause

it to have finer hydride particles. It was favorable to form the nano-phase composite. The micro-morphology, crystal structures and non-/isothermal de-/hydrogenation properties of the MgH_2-$Ti_6Cr_{14}V_{80}Ce_1H_x$ composite were systematically investigated.

2. Experimental Section

2.1. Preparation of $Ti_6Cr_{14}V_{80}Ce_1$ Hydrogen-Storage Alloy

The raw materials 0.5491 g Ti (sponge, 99.9%), 1.3918 g Cr (granules, 99.9%), 7.7912 g V (granules, 99.8%) and 0.2732 g Ce (bulk, 99.8%, an additional 2 wt% Ce added to reduce Ce losses) were selected to prepare as-cast $Ti_6Cr_{14}V_{80}Ce_1$ alloys (designed as 10 g/pcs) fabricated via non-consumable vacuum arc melting within a water-cooled copper crucible in an argon atmosphere (−0.5 bar) purified via individual Ti melting to minimize oxygen content. To ensure chemical homogeneity, each ingot was subjected to a melting current of 120–140 A, repeatedly flipped over and smelted four times.

2.2. Synthesis of MgH_2-$Ti_6Cr_{14}V_{80}Ce_1H_x$ Composites

The prepared $Ti_6Cr_{14}V_{80}Ce_1$ ingot was polished with an electric grinder to remove impurities and oxide layers. A part of each of them was then mechanically crushed into chips then loaded into the 250 mL stainless-steel jar, which was charged with 40.0 bar hydrogen and transformed into planetary ball mill equipment. The $Ti_6Cr_{14}V_{80}Ce_1$ chips were ball milled with the following procedure: 400 rpm with a stainless-steel ball (80% diameter ϕ 6 mm, 20% diameter ϕ 10 mm) with a weight ratio, i.e., ball to sample ratio, equal to 40:1. This was continuously performed for 1 h and then we went back to the glovebox to take out the synthesized hydrogenated $Ti_6Cr_{14}V_{80}Ce_1$ powder (named $Ti_6Cr_{14}V_{80}Ce_1H_x$). The commercial MgH_2 (98 wt%, Shanghai Mg Power Technology Ltd., Shanghai, China) +*y* wt% $Ti_6Cr_{14}V_{80}Ce_1H_x$ (*y* = 0, 3, 5, 10, 15) composites were synthesized via ball milling in 50.0 bar H_2 at 450 rpm for 8 h. The ball to sample weight ratio was set as 80:1 (milling balls were set as 80% diameter ϕ 6 mm, 20% diameter ϕ 10 mm). To avoid local overheating, this was implemented by alternating milling for 12 min, followed by a pause of 6 min. All the powder sample handling was carried out in an Ar-filled glovebox (Etelux Lab 2000, Beijing, China), where the contents of O_2 and H_2O were kept below 0.1 ppm.

2.3. Characterization of Materials

The microcrystal structure and phase composition of the prepared samples were analyzed via X-ray diffraction (XRD, PANalytical X'Pert, Almelo, The Netherlands) using Cu Kα radiation (40 kV, 40 mA). The powders including Mg/MgH_2 were covered with a polyimide film to prevent the oxidization and spontaneous ignition of Mg/MgH_2 during transfer and testing. The micro-morphology and compositional analysis were characterized via a field emission scanning electron microscope (SEM, JEOL JSM-IT800, Tokyo, Japan) along with energy dispersive spectroscopy (EDS). The microscopic morphology and microstructure information were obtained via a high-transmission electron microscope (TEM, FEI Talos-F200s, Waltham, MA, USA) equipped with an energy dispersive X-ray spectrometer (EDS). The thermodynamic properties were measured using differential scanning calorimetry (DSC, Netzsch STA 449F3, Bavaria, Germany) at the heating rate of 2 °C·min^{-1} with Ar as the purge gas.

For hydrogen-storage performance testing, the kinetics and pressure–composition–temperature (PCT) curves of the $Ti_6Cr_{14}V_{80}Ce_1$ alloy were determined by utilizing a Sievert-type apparatus (MH-PCT, GRIMAT Engineering Institute, Beijing, China) over a temperature range of 5~65 °C. A constant temperature could be maintained with the circulating water bath (DC-2006, Tenlin, Yancheng, China). The $Ti_6Cr_{14}V_{80}Ce_1H_x$ catalyzed MgH_2 composites' isothermal de-/rehydrogenation curves were tested using a Sievert-type apparatus (ZDHM-4, Zhejiang University, Hangzhou, China). For non-isothermal experiments, the composite was heated with a heating rate of 2 °C·min^{-1} using a resistance furnace in a vacuum. The isothermal hydrogen de-/rehydrogenation experiments were carried out at 0.001 bar for dehydrogenation and an initial hydrogen pressure of 50.0 bar

for rehydrogenation. Moreover, the PCT curves and cyclic hydrogen de-/absorption tests of the composites were measured at corresponding temperatures via a commercialized Sievert's apparatus (HPSA-autoPro device, Shanghai, China) along with loading approximately 150 mg of the sample for each test. Cyclic tests were performed at 300 °C and the duration of each was 10 min for de-/rehydrogenating. The above-mentioned Sievert's apparatus was calibrated by loading 1g commercial $LaNi_5$ powder for measuring the hydrogen de-/absorption kinetics and pressure–composition–isothermal temperature (P-C-I) curves based on the test method outlined in GB/T 33291-2016 [35].

3. Results and Discussion

3.1. The Structural and Morphological Characterization

Figure 1a shows the XRD patterns of the as-cast $Ti_6Cr_{14}V_{80}Ce_1$ alloy and the obtained $Ti_6Cr_{14}V_{80}Ce_1H_x$ samples after pre-ball milling. It can be found that the prepared $Ti_6Cr_{14}V_{80}Ce_1$ alloy presents the single BCC phase with a lattice constant of 3.025 Å. The phase structure of the hydrogenated state $Ti_6Cr_{14}V_{80}Ce_1H_x$ powder after pre-ball milling in a hydrogen atmosphere transformed into an FCC phase ascribed to the formation of the VH_2 phase, which has been reported in the corresponding literature studies [36,37]. Actually, the BCT phase was presented in the ball milled $Ti_6Cr_{14}V_{80}Ce_1$ sample (in Figure 1a), was attributed to the generation of the V_2H phase and can be explained from the measured PCT curves at ambient conditions (shown in Figure S1). The occurrence of hysteresis was attributed to severe lattice deformation and dislocation existing at the interface of the solution phase (α-phase) and the hydride phase (β-phase) due to the different equilibrium volumes of their unit cells resulting from their respective hydrogen accommodation conditions [38,39]. That is, the hysteresis is considered to be derived from the deformation strain and stress due to the unit cell volume contraction and expansion during the dynamic hydrogen sorption process. In addition, the as-cast $Ti_6Cr_{14}V_{80}Ce_1$ alloy was observed via SEM and the elemental compositions were also identified, as shown in Figure 1c. The EDS results show that each element was homogeneously distributed in the alloy, and the actual composition coincided with the nominal composition. Moreover, it shows that the $Ti_6Cr_{14}V_{80}Ce_1H_x$ powders were composed of several submicron-sized particles in SEM image (Figure S2a). The XRD patterns of the ball milled MgH_2-y wt%$Ti_6Cr_{14}V_{80}Ce_1H_x$ (y = 0, 3, 5, 10, 15) composite were shown in Figure 1b, which shows that the compound was composed of the dominant phase of β-MgH_2 and a small BCT phase from $Ti_6Cr_{14}V_{80}Ce_1H_x$. In addition, a small γ-MgH_2 phase was also detected in the composite. The XRD patterns of the ball milled MgH_2 and pure MgH_2 are also compared in Figure S3. The figure indicates that the diffraction peaks of the ball milled state of MgH_2 subjected to ball milling for a long time became broader than pure MgH_2. Zhang et al. [40] also reported similar results in MgH_2-20 wt%$Ti_{0.16}Cr_{0.24}V_{0.6}$ powder synthesized via reactive ball milling. To better uncover morphology information, the ball milled MgH_2-10 wt%$Ti_6Cr_{14}V_{80}Ce_1H_x$ composite was observed. Figure S2b shows that many micro/nano-sized $Ti_6Cr_{14}V_{80}Ce_1H_x$ particles were embedded in the MgH_2 substrate.

The micro phase and morphology details of the ball milled MgH_2-10 wt%$Ti_6Cr_{14}V_{80}Ce_1H_x$ composite were further characterized via TEM and HRTEM, as shown in Figure 2. Figure 2a shows that there are different interplanar spacings corresponding to the different phase structures identified in the composite. Lattice fringes with interplanar spacings of 2.501 Å and 2.490 Å can be determined to be the (101) planes of β-MgH_2. The corresponding selected area diffraction pattern (SADP) from Figure 2b is also displayed in Figure 2c, which demonstrates there was β-MgH_2 and BCC phase of $Ti_6Cr_{14}V_{80}Ce_1$. The corresponding EDS elemental mapping images were also produced and we demonstrated that Ti, Cr, V and Ce elements are homogeneously distributed on the surface of MgH_2 powder. According to the Mg, Ti, Cr, V and Ce elemental mappings results, it can be inferred that the $Ti_6Cr_{14}V_{80}Ce_1H_x$ located in the glossy white area was uniformly dispersed in the MgH_2 substrate from the dark area in the HAADF image (in Figure 2d).

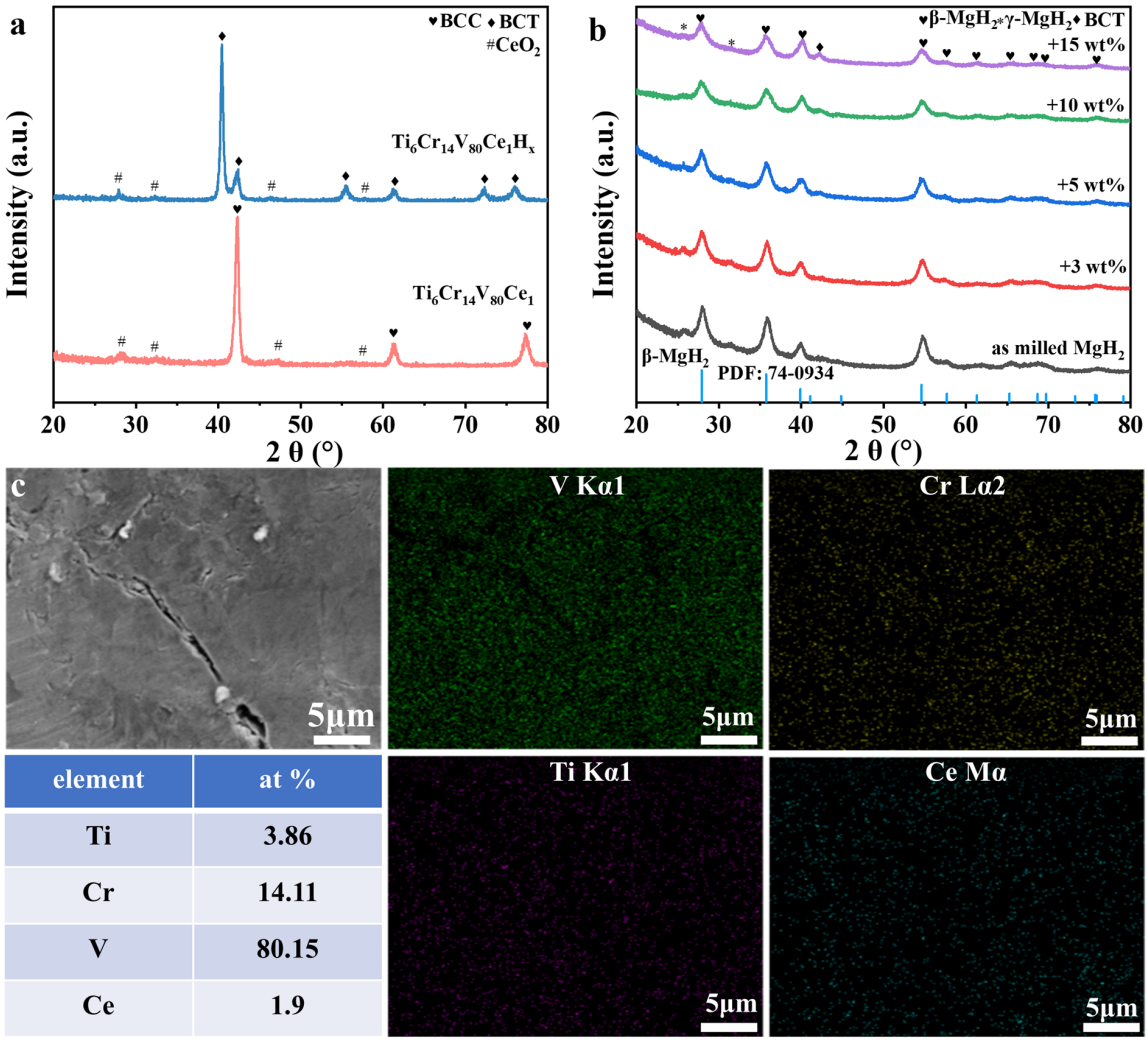

element	at %
Ti	3.86
Cr	14.11
V	80.15
Ce	1.9

Figure 1. XRD patterns of the as-cast $Ti_6Cr_{14}V_{80}Ce_1$ alloy and the $Ti_6Cr_{14}V_{80}Ce_1H_x$ hydride by pre-ball milled under hydrogen pressure (**a**); XRD patterns of the ball milled MgH_2-*y* wt%$Ti_6Cr_{14}V_{80}Ce_1H_x$ (*y* = 3, 5, 10, 15) composite (**b**); scanning electron microscopy (SEM)-EDS analysis of the $Ti_6Cr_{14}V_{80}Ce_1$ alloy (**c**).

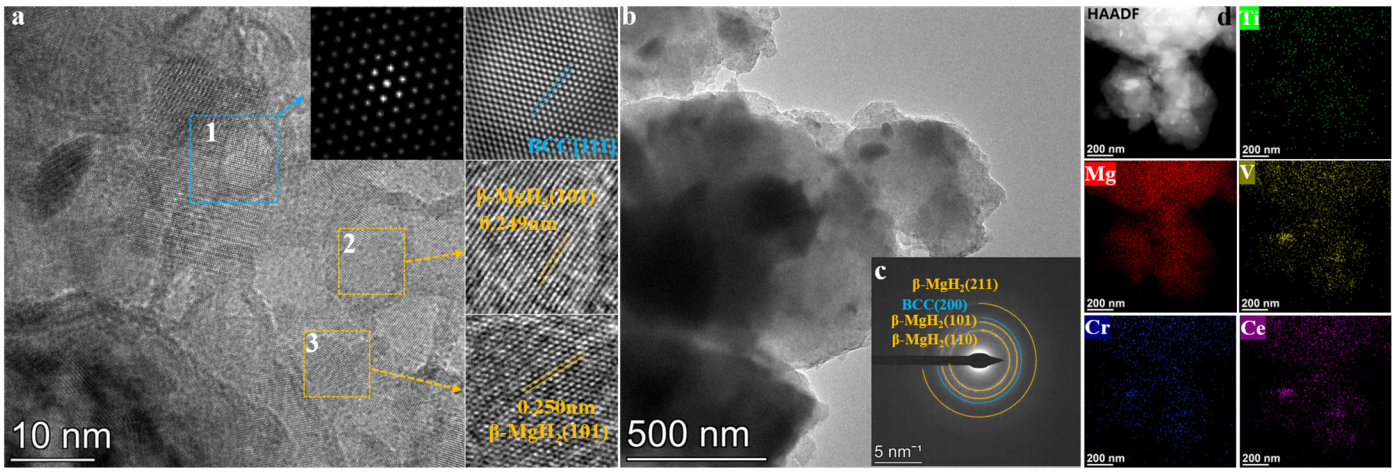

Figure 2. The HRTEM images (**a**,**b**) and the SADP image (**c**) and the corresponding EDS mapping images (**d**) of the MgH_2- 10 wt%$Ti_6Cr_{14}V_{80}Ce_1H_x$ composite.

3.2. Hydrogen de-/Absorption Properties

The $Ti_6Cr_{14}V_{80}$ alloy after Ce doping has a superior ability to rapidly absorb hydrogen at room temperature without going through activation at 400 °C. This is because cerium can effectively reduce the oxygen concentration in the alloy. Figure 3 presents the hydrogen de-/absorption kinetics curves of the $Ti_6Cr_{14}V_{80}Ce_1$ alloy at 5–65 °C without any activation through a high-temperature process. It can be evidently observed that there is a very short initial incubation period for absorbing kinetics in Figure 3a. The $Ti_6Cr_{14}V_{80}Ce_1$ alloy can rapidly absorb 3.7 wt% H_2 at 25 °C within 15 min. However, the maximum hydrogen absorption capacity at 65 °C is approximately 2.3 wt%. In addition, we measured the hydrogen-absorption properties of the undoped-Ce $Ti_6Cr_{14}V_{80}$ alloy when processed by ball milling; the measurement suggests that it is unable to absorb hydrogen. In addition, the desorption kinetics curves at the corresponding temperature of the $Ti_6Cr_{14}V_{80}Ce_1$ alloy after absorption saturation are shown in Figure 3b. The dehydrogenation capacity of the alloy reaches 1.32, 2.10, 1.90 and 0.91 wt% within 30 min at 5, 25, 45 and 65 °C, respectively. It can be observed that the hydrogen capacity decreases when the temperature increases. This is because the hydrogen absorption of the alloy is an exothermic reaction while the hydrogen desorption process is an endothermic reaction. From the PCT curves (shown in Figure S1), it can be seen that the content of the residual hydrogen can almost be matched, which is derived from the V_2H phase being difficult to release. This is in good agreement with relevant reports.

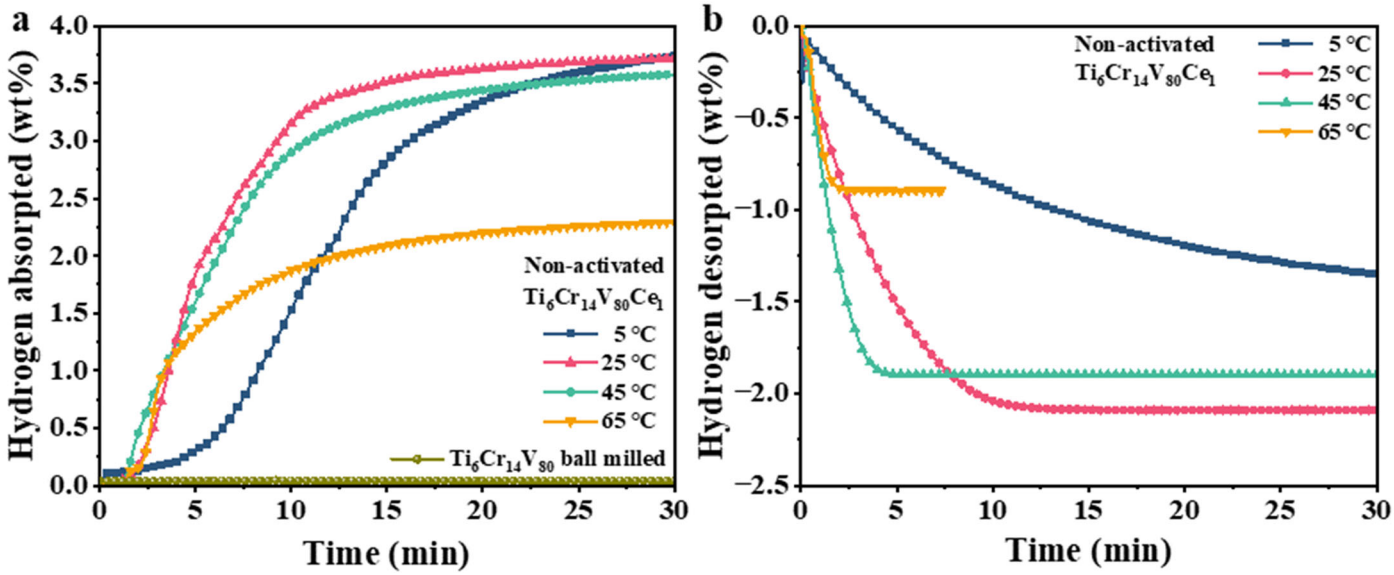

Figure 3. The hydrogen-absorption (**a**) and -desorption (**b**) curves of the $Ti_6Cr_{14}V_{80}Ce_1$ alloy at 5–65 °C without activation through high temperature.

To evaluate the catalytic effects of the $Ti_6Cr_{14}V_{80}Ce_1H_x$ alloy compounded with MgH_2, non-/isothermal hydrogen-desorption curves of the corresponding composites were constructed. Figure 4a displays the temperature programmed desorption (TPD) curves of the composites, and demonstrates that the initial dehydrogenated temperature was reduced to approximately 160 °C when the $Ti_6Cr_{14}V_{80}Ce_1H_x$ powder was incorporated. However, there is a slight distinction in the initial dehydrogenated temperature when different amounts of $Ti_6Cr_{14}V_{80}Ce_1H_x$ were introduced. Further, the DSC curves at a heating rate of 2 °C·min^{-1} for the MgH_2-$Ti_6Cr_{14}V_{80}Ce_1H_x$ composite are also displayed in Figure 4b; the peak dehydrogenated temperature was identified as 265.6, 258.8, 254.3 and 257.2 °C for MgH_2-3 wt%$Ti_6Cr_{14}V_{80}Ce_1H_x$, MgH_2-5 wt%$Ti_6Cr_{14}V_{80}Ce_1H_x$, MgH_2-10 wt%$Ti_6Cr_{14}V_{80}Ce_1H_x$ and MgH_2-15 wt%$Ti_6Cr_{14}V_{80}Ce_1H_x$, respectively. These results suggest the incorporation of $Ti_6Cr_{14}V_{80}Ce_1H_x$ remarkably enhances the dehydrogenation performance of MgH_2.

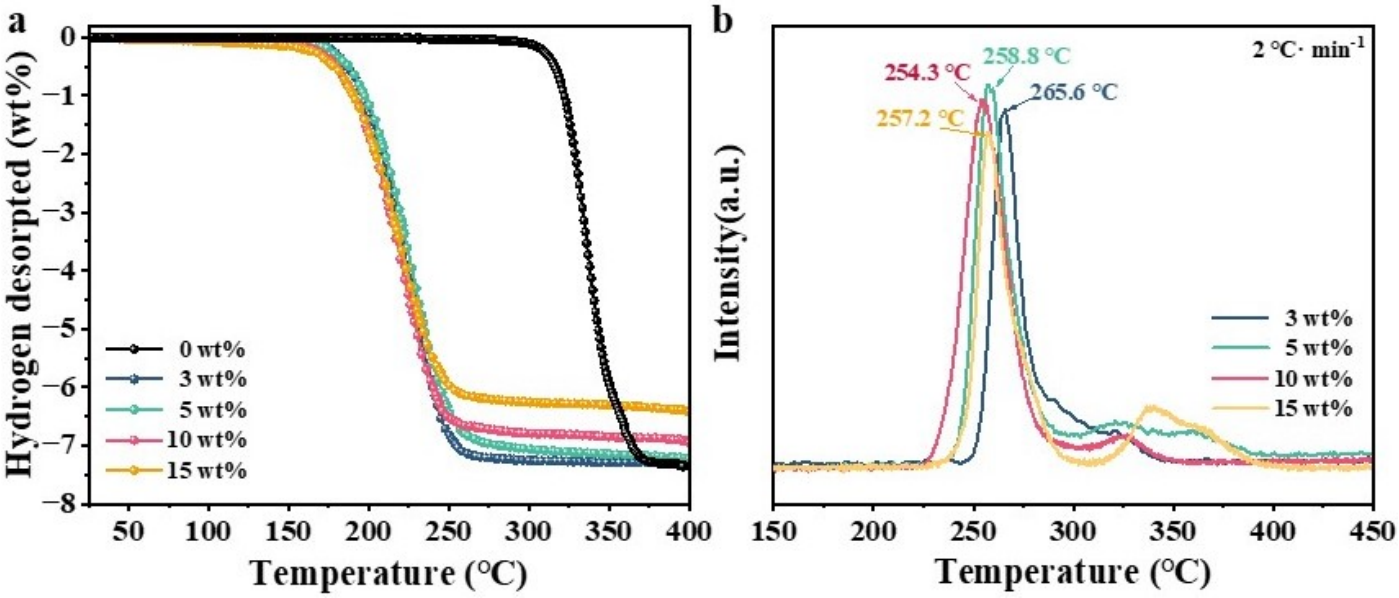

Figure 4. Non-isothermal dehydrogenation curves of the MgH_2-*y* wt%$Ti_6Cr_{14}V_{80}Ce_1H_x$ (*y* = 0, 3, 5, 10, 15) composites (**a**); DSC curves of the MgH_2-*y* wt%$Ti_6Cr_{14}V_{80}Ce_1H_x$ (3, 5, 10, 15) composites at a heating rate of 2 °C·min^{-1} (**b**).

Figure 5a shows the isothermal hydrogen-absorption curves of the MgH_2-10 wt% $Ti_6Cr_{14}V_{80}Ce_1H_x$ composite. It shows that 2.0 wt% H_2 could be uptaked within 1 h even at room temperature and 4.86 wt% H_2 was recharged within 10 s at 125 °C. Figure 5b–f demonstrate the isothermal dehydrogenation curves for the MgH_2-*y* wt%$Ti_6Cr_{14}V_{80}Ce_1H_x$ (*y* = 0, 3, 5, 10, 15) composite at various temperatures. Hydrogen could be liberated from the ball milled pristine MgH_2 when the procedure was performed at above 275 °C, as illustrated in Figure 5b. When 3 wt% $Ti_6Cr_{14}V_{80}Ce_1H_x$ was introduced (shown in Figure 5c), the composite can release 6.60 and 6.85 wt% H_2 within 20 min at 230 and 250 °C, respectively. In addition, the MgH_2-5 wt% $Ti_6Cr_{14}V_{80}Ce_1H_x$ composite can release 6.91 and 7.15 wt% H_2 within 12 min at 230 and 250 °C (depicted in Figure 5d), respectively. It is worth noting that, as illustrated in Figure 5e, the dehydrogenation capacity reached 6.67 wt% °C at 230 °C for 8 min and at 250 °C for 5 min when 10 wt% $Ti_6Cr_{14}V_{80}Ce_1H_x$ was added into MgH_2. Furthermore, the duration was 8 min for complete dehydrogenation capacity of 6.2 wt% at 250 °C in the MgH_2-15 wt% $Ti_6Cr_{14}V_{80}Ce_1H_x$ composite, as presented in Figure 5f. The above-mentioned results reveal that the $Ti_6Cr_{14}V_{80}Ce_1H_x$ catalysts with varying addition amounts can significantly accelerate the liberation of hydrogen of MgH_2, and the total amount of hydrogen desorption decreased as $Ti_6Cr_{14}V_{80}Ce_1H_x$ increased. Overall, the MgH_2-10 wt%$Ti_6Cr_{14}V_{80}Ce_1H_x$ composite demonstrated the best catalytic effect based on the desorption rate and amount of hydrogen at varying temperatures.

To further study the dehydrogenated reaction kinetics of the $Ti_6Cr_{14}V_{80}Ce_1H_x$-modified MgH_2, it is essential to analyze kinetic models during the de-/absorption process. In general, with the classical Johnson–Mehl–Avrami–Kolmogorov (JMAK) model, the nucleation and growth mechanism is suitable for describing the hydrogen de-/absorption behaviors [41,42]. Equation (1) is as follows:

$$\ln[-\ln(1-\alpha)] = n\ln k + n\ln t \quad (1)$$

where α is the reaction fraction via t (α is the ratio of de-/absorption to the total capacity at any moment), k is the rate constant of hydrogen de-/absorption. n is the Avrami exponent for reaction order. k can be obtained from the intercept by establishing the linear relationship between $\ln[-\ln(1-\alpha)]$ and $\ln t$.

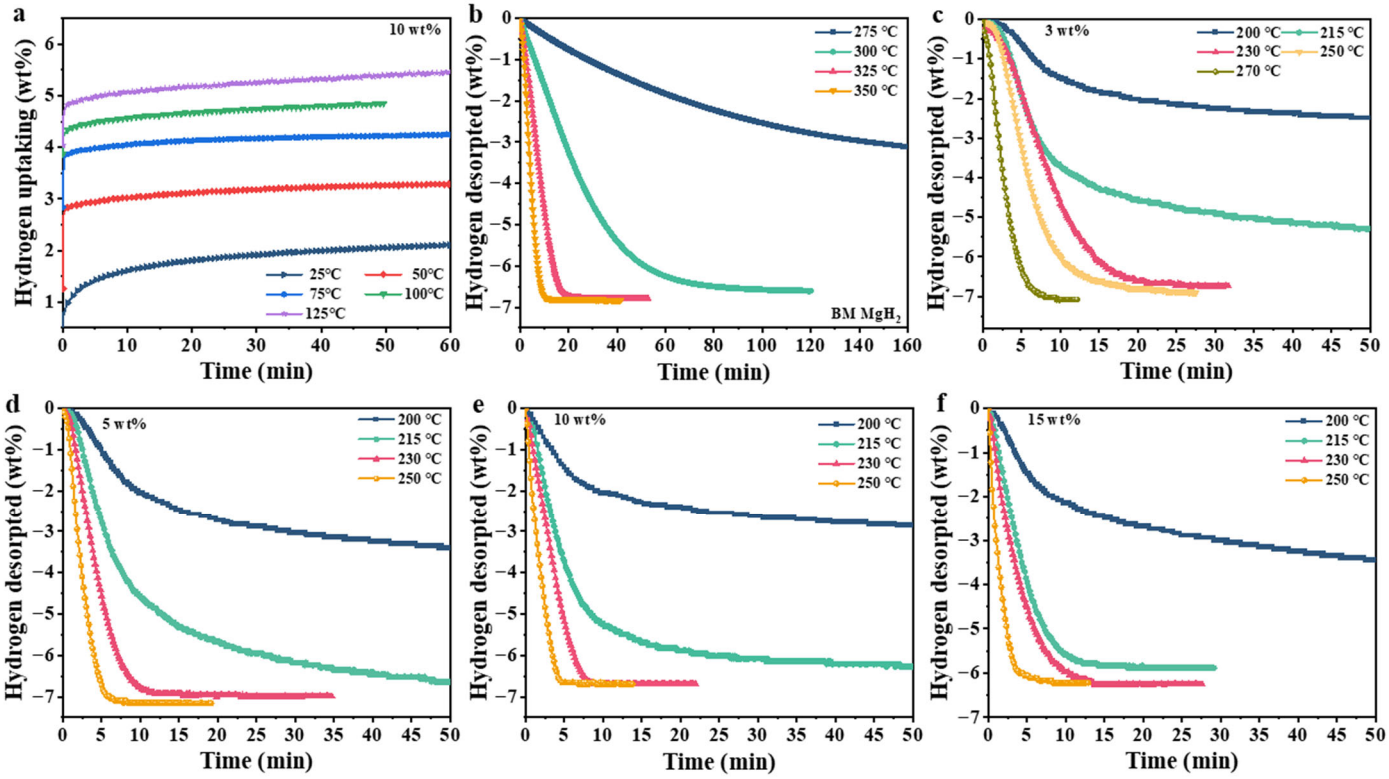

Figure 5. Isothermal rehydrogenation curves of the MgH_2-10 wt%$Ti_6Cr_{14}V_{80}Ce_1H_x$ composite at different temperature (**a**); isothermal dehydrogenation curves of MgH_2 (**b**), the MgH_2-3 wt%$Ti_6Cr_{14}V_{80}Ce_1H_x$ (**c**), MgH_2-5 wt%$Ti_6Cr_{14}V_{80}Ce_1H_x$ (**d**), MgH_2-10 wt%$Ti_6Cr_{14}V_{80}Ce_1H_x$ (**e**) and MgH_2-15 wt%$Ti_6Cr_{14}V_{80}Ce_1H_x$ (**f**) composites.

Thus, the activation energy (E_a) of the composite during the de-/absorption process can be achieved through the Arrhenius Formulas (2) and (3):

$$k = Ae^{-\frac{E_a}{RT}} \quad (2)$$

$$\ln k = -\frac{E_a}{RT} + \ln A \quad (3)$$

where A is the pre-exponential factor and E_a is the activation energy. By plotting $\ln k$ (calculated from Equation (1)) against $1/T$, the E_a can be evaluated. In accordance with the isothermal dehydrogenated kinetics experimental data in Figure 5b–f, we plotted the data with $0.2 < \alpha < 0.8$ at different temperatures. Figure 6a–e exhibit the JMAK model fitting results of $\ln[-\ln(1-\alpha)]$ vs. $\ln t$ for dehydrogenation of the MgH_2-y wt%$Ti_6Cr_{14}V_{80}Ce_1H_x$ (y = 0, 3, 5, 10, 15) composites at the corresponding temperatures. It can be seen that the reaction order (n, the slope) value for dehydrogenation is approximately 1~2, which infers that the dehydrogenated rate-limiting steps of the composite are determined to be the diffusion-controlled growth model [43]. After fitting the $\ln k$ vs. $1000/T$ values, the apparent dehydrogenated activation energies (E_a) of the relative composites were calculated and are presented in Figure 6f. It was found that the E_a of the compos-

ites with non-/doping, 3, 5, 10, 15 wt% $Ti_6Cr_{14}V_{80}Ce_1H_x$ is 119.56 ± 4.9, 83.89 ± 2.1, 65.54 ± 1.1, 62.62 ± 5.1 and 71.90 ± 6.8 kJ·mol$^{-1}H_2$, respectively. It can be found that the MgH_2-10 wt%$Ti_6Cr_{14}V_{80}Ce_1H_x$ composite exhibits the lowest dehydrogenated activation energy during them. Obviously, the introduction of the $Ti_6Cr_{14}V_{80}Ce_1H_x$ catalyst can significantly decrease the E_a of MgH_2; in particular, the E_a is reduced by 52% when doping with 10 wt%$Ti_6Cr_{14}V_{80}Ce_1H_x$. The comparison of the corresponding reported catalyst-modified MgH_2 is listed in Table S1.

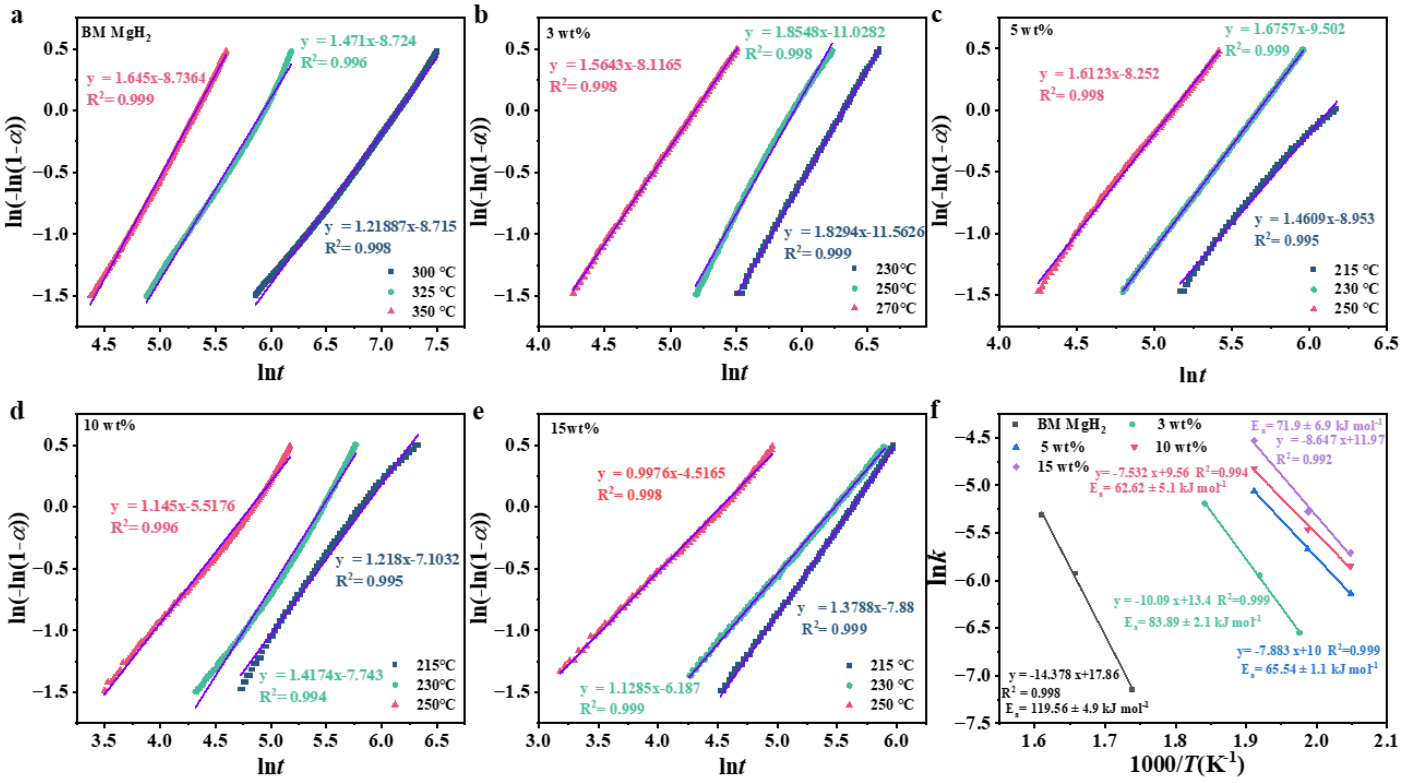

Figure 6. JMAK fitting results (0.2 < α < 0.8 at different temperatures) of the MgH_2-*y* wt%$Ti_6Cr_{14}V_{80}Ce_1H_x$ (*y* = 0, 3, 5, 10, 15) composites based on the isothermal desorption experimental data (**a**–**e**); the calculated dehydrogenated activation energies (E_a) via Arrhenius plots (ln*k* vs. 1000/*T* plots) of the corresponding composites (**f**).

Reversable isothermal de-/rehydrogenation tests were performed covering 100 cycles to evaluate the cyclic stability of the MgH_2-10 wt%$Ti_6Cr_{14}V_{80}Ce_1H_x$ composite at 300 °C with the initial hydrogen pressure of 50.0 bar. Figure 7a,b depicted that the composite maintains 84% retention along with the first dehydrogenated capacity of 6.28 wt% and the final dehydrogenated capacity of 5.27 wt% after 100 cycles. The loss of the hydrogen capacity was ascribed to the residual hydrogen generated from the $Ti_6Cr_{14}V_{80}Ce_1$ catalyst, which could not be completely released within 15 min. The desorption kinetics of the first, 10th, 50th and 100th cycles of the composite are shown in Figure 7c; it was found that the dehydrogenation rate after several cycles was obviously accelerated. Therefore, it can be deduced that the 'autocatalytic effect' originating in $Ti_6Cr_{14}V_{80}Ce_1H_x$ plays a crucial role in boosting the de-/hydrogenation performance of MgH_2.

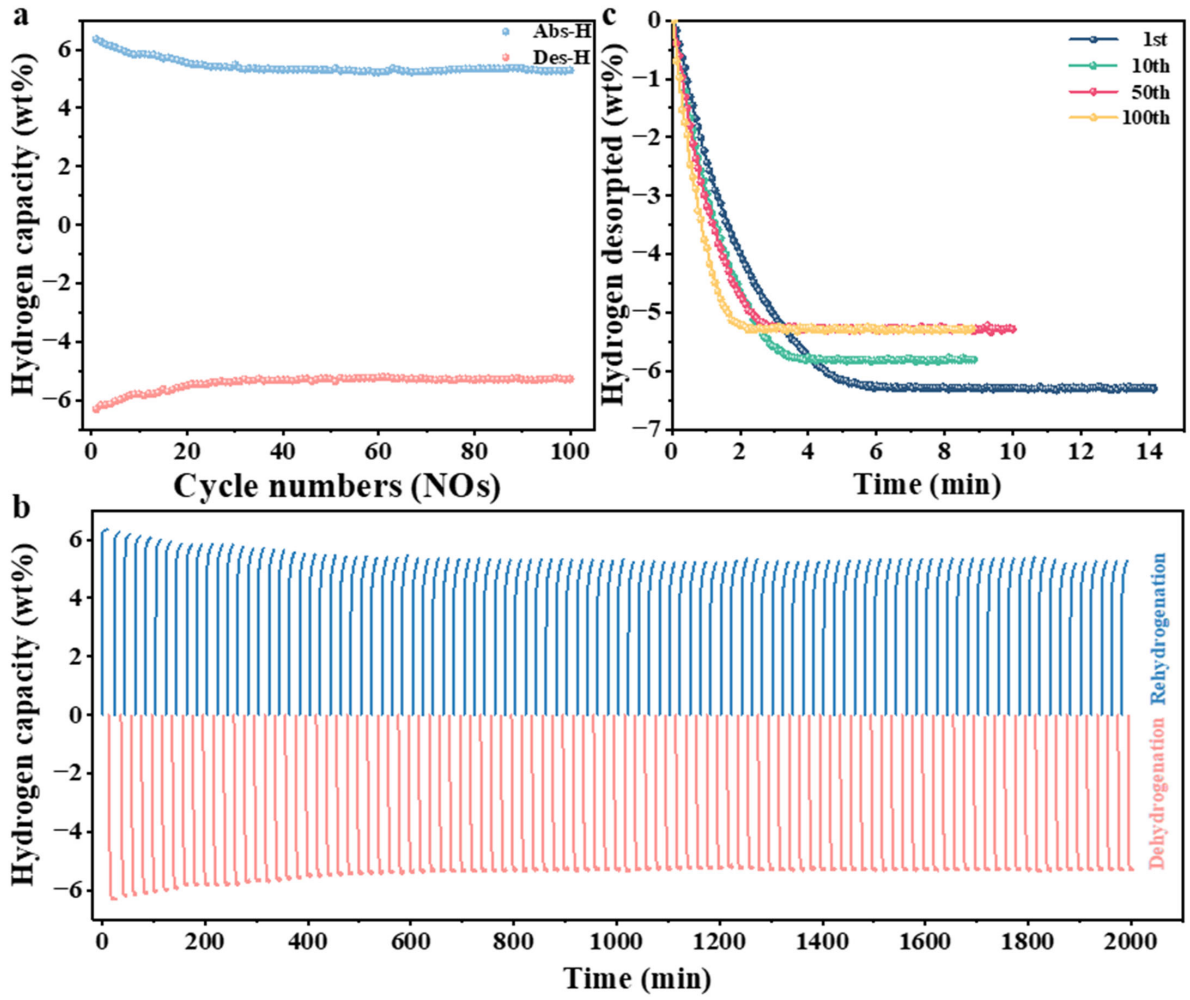

Figure 7. One-hundred cycles of hydrogen absorption and desorption of the MgH_2-10 wt%$Ti_6Cr_{14}V_{80}Ce_1H_x$ composite (**a**,**b**); the desorption kinetic curves of the 1st, 10th, 50th and 100th cycles of the MgH_2-10 wt%$Ti_6Cr_{14}V_{80}Ce_1H_x$ composite after dehydrogenation (**c**).

3.3. The Catalytic Mechanism

To further explore the catalytic mechanism of the remarkable hydrogen de-/absorption kinetics from the $Ti_6Cr_{14}V_{80}Ce_1H_x$-catalyzed MgH_2, XRD and TEM were applied to elucidate the structure evolution of $Ti_6Cr_{14}V_{80}Ce_1H_x$ at different states. The XRD pattern results of the ball milled de-/re-hydrogenated state of the 10 wt% $Ti_6Cr_{14}V_{80}Ce_1H_x$-catalyzed MgH_2 are shown in Figure 8a. The BCT phase of the alloy naturally emerged in the ball milled composite due to its desorption plateau pressure features, which is confirmed in Figure S1. Although β-MgH_2 has undisputedly become the dominant phase of the ball milled and rehydrogenated state, some Mg phases could be detected in the hydrogenated sample. This was because the interior of an Mg particle is not easily fully hydrogenated due to the agglomeration phenomenon. $Ti_6Cr_{14}V_{80}Ce_1H_x$ after dehydrogenation will transform into a BCC phase and return to a FCC phase when rehydrogenated. Furthermore, the XRD results of the 10 wt% $Ti_6Cr_{14}V_{80}Ce_1H_x$-catalyzed MgH_2 after the different dehydrogenated temperatures are depicted in Figure 8b. It can be clearly observed that there is a peak located at 42 ° which corresponds to the (110) plane of the BCC phase from the $Ti_6Cr_{14}V_{80}Ce_1$ alloy. It is also proved that $Ti_6Cr_{14}V_{80}Ce_1H_x$ has a superior catalytic effect on dissociation of Mg-H bonds even at 200 °C, as reflected in the XRD patterns.

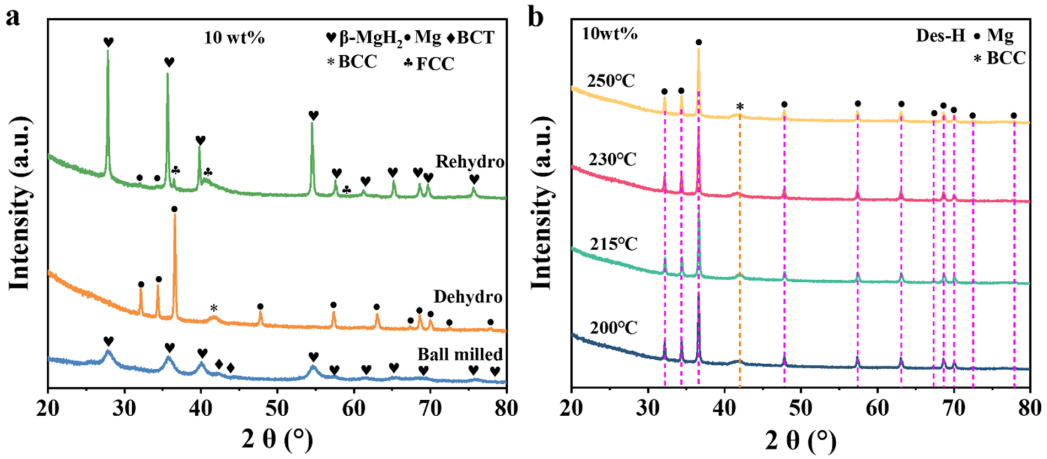

Figure 8. XRD patterns of the ball milled, rehydrogenated, dehydrogenated state of the MgH_2-10 wt%$Ti_6Cr_{14}V_{80}Ce_1H_x$ composite (**a**); XRD patterns of the MgH_2-10 wt%$Ti_6Cr_{14}V_{80}Ce_1H_x$ composite under different dehydrogenated temperatures (**b**).

To further investigate the microstructural characteristics of the composite, TEM observations on the dehydrogenated composite were obtained. As shown in Figure 9a,b, the Mg phase ($P6_3/mmc$ (194)) is observed in HRTEM images (Figure 9c) with lattice spacing of 0.245 nm. Besides, it can be also observed that there are apparent interfaces between Mg and the $Ti_6Cr_{14}V_{80}Ce_1$ with the BCC phase in Figure 9c. As depicted in Figure 9d, the diffraction spot lattice of the Fourier transform pattern exhibits the typical BCC phase (110) zone axis. Furthermore, it can be clearly observed that there are jointed interfaces from Mg and BCC phases, which presents the obvious layer fault in HRTEM images (Figure 9c). This suggests that massive dislocation defects were generated during the high-energy ball milling. Figure 9e shows the angle annual dark-field (HAADF) images of the dehydrogenated sample and the corresponding EDS mappings. It can be seen that the $Ti_6Cr_{14}V_{80}Ce_1$ particles with an average grain size of 200 nm are dispersed in the Mg/MgH_2 matrix. The Ti, V, Cr and Ce elements were homogeneously distributed on the surface of Mg/MgH_2. The brighter nanoparticles are considered as the $Ti_6Cr_{14}V_{80}Ce_1$ alloy introduced in the MgH_2.

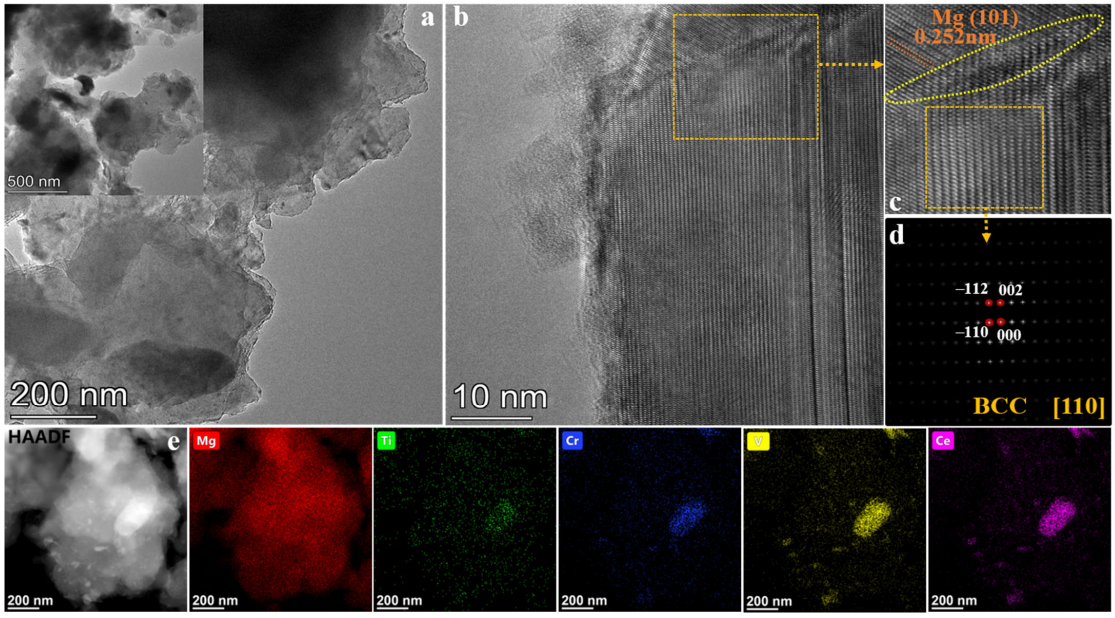

Figure 9. The TEM and HRTEM images (**a**–**c**), the corresponding FFT image (**d**), the HAADF image (**e**) and the corresponding EDS mapping of the dehydrogenated MgH_2-10 wt%$Ti_6Cr_{14}V_{80}Ce_1H_x$ composite.

Based on the above discussions, the catalytic process of the $Ti_6Cr_{14}V_{80}Ce_1H_x$ compounded with MgH_2 can be speculated on. The pre-ball milled $Ti_6Cr_{14}V_{80}Ce_1$ alloy transformed into $Ti_6Cr_{14}V_{80}Ce_1H_x$ hydrides under hydrogen pressure. The obtained $Ti_6Cr_{14}V_{80}Ce_1H_x$ ball milled with MgH_2 stayed as the BCT phase in the composite in ambient conditions. After dehydrogenation, the catalyst $Ti_6Cr_{14}V_{80}Ce_1H_x$ transformed into the BCC phase and returned into the FCC phase when it was rehydrogenated. The structure evolution of the $Ti_6Cr_{14}V_{80}Ce_1$ alloy was in accordance with that of the reported V-based BCC-type hydrogen-storage alloys [44,45]. In terms of the hydrogen-storage alloy with the BCC phase, the inherent features of superior de-/absorption kinetics contribute to the remarkable catalytic effect on MgH_2. We called it the 'autocatalytic effect' of the hydrogen-storage alloy, and it had a fast de-/absorption rate and was the priority of the hydrogen diffusion during the hydrogen dissociation and recombination in the composite. The autocatalytic reaction was also reported by Zhu et al. [46]. They studied melted $MmNi_{5-x}(CoAlMn)_x$ alloy milling with Mg to form a nano-phase composite by fitting the kinetic curve and found that it matched with the rate equation of the autocatalysis process. On one hand, the $Ti_6Cr_{14}V_{80}Ce_1H_x$ nano-particles act as the active sites to de-/absorb hydrogen and dissociate from H atoms. The de-/absorption behavior of the $Ti_6Cr_{14}V_{80}Ce_1H_x$ particles can thus trigger the migration of H atoms into the Mg/MgH_2 matrix. One the other hand, the generated plentiful dislocations offer extra stacking fault energy and distortion energy, which provide massive hydrogen diffusion channels in the composite. The elements Ti, Cr, V and Ce of $Ti_6Cr_{14}V_{80}Ce_1H_x$ have lower electronegativity than Mg, which significantly weakens the Mg-H bonds and further facilitates the dehydrogenation reaction. Consequently, the favorable self-absorption or desorption hydrogen kinetics characteristics from the $Ti_6Cr_{14}V_{80}Ce_1H_x$ particles and the structure transitions significantly enhance the de-/hydrogenation kinetic performance of MgH_2.

4. Conclusions

The Ce-doped $Ti_6Cr_{14}V_{80}Ce_1$ hydrogen-storage alloy was prepared via arc melting and hydrogenated into $Ti_6Cr_{14}V_{80}Ce_1H_x$ hydrides via ball milling in a hydrogen atmosphere. The MgH_2 + y wt%$Ti_6Cr_{14}V_{80}Ce_1H_x$ (y = 0, 3, 5, 10, 15) nano-composites were prepared via ball milling to explore the catalytic effect of the $Ti_6Cr_{14}V_{80}Ce_1H_x$ alloy on the hydrogen de-/absorption properties of MgH_2. Experimental results exhibit that the 10 wt% $Ti_6Cr_{14}V_{80}Ce_1H_x$-catalyzed MgH_2 showed an initial dehydrogenated temperature of 160 °C and can absorb 2.0 wt% H_2 within 1 h at room temperature. Moreover, the composite can rapidly release 6.73 wt% H_2 within 8 min at 230 °C. Meanwhile, the composite has a reversible de-/absorption hydrogen capacity retention of 84% after 100 cycles at 300 °C. In addition, the calculated dehydrogenated activation energy of the composite via the JMAK model was identified to be 62.62 kJ mol^{-1}. A catalytic mechanism analysis revealed that the reversible phase transformation (BCC-FCC) originating in the $Ti_6Cr_{14}V_{80}Ce_1H_x$ hydrides can offer more diffusion pathways for hydrogen migration and act as the active nucleation sites for Mg/MgH_2. In addition, plentiful of dislocations and defects originating in the connected interfaces from $Ti_6Cr_{14}V_{80}Ce_1H_x$ and MgH_2 can provide extra interface energy and effectively weaken the Mg-H bonds. This work offers an effective strategy for fabricating a hydrogen-storage alloy compounded with MgH_2 with superior hydrogen sorption kinetics characteristics.

Supplementary Materials: The following supporting information can be downloaded at: https://www.mdpi.com/article/10.3390/met14050572/s1, Figure S1. The PCT curves of the as-cast $Ti_6Cr_{14}V_{80}Ce_1$ alloys at the different temperature. Figure S2. The SEM image of the $Ti_6Cr_{14}V_{80}Ce_1H_x$ hydride by pre-ball milled under hydrogen pressure (a); The SEM image and EDS mapping results of the ball milled MgH_2-10 wt%$Ti_6Cr_{14}V_{80}Ce_1H_x$ composite (b). Figure S3. The XRD patterns of the pure MgH_2 and the ball milled MgH_2. Table S1. Comparison of different catalysts-doped on dehydrogenation kinetics of MgH_2. Refs. [32,42,47–49] are cited in the Supplementary Materials.

Author Contributions: Conceptualization, H.X. and X.Z.; methodology, H.X. and Y.L.; validation, L.Y.; formal analysis, H.X., X.Z. and C.L.; investigation, H.X., C.M. and Y.L.; resources, R.W. and Q.C.; data curation, X.Z. and C.L.; writing—original draft preparation, H.X.; writing—review and editing, Q.C. and L.Y.; visualization, C.M.; supervision, Q.C.; project administration, Q.C. and R.W.; funding acquisition, Q.C. All authors have read and agreed to the published version of the manuscript.

Funding: This work was funded by National Key Research and Development program of China (2022YFB3504700), Jiangxi Provincial Natural Science Foundation (No. 20212ACB213009) and Ganzhou "Jiebangguashuai" Program (NO.2023ULGX0002). This work was also supported by a grant from the Research Projects of Ganjiang Innovation Academy, Chinese Academy of Sciences (No. E355B0020).

Data Availability Statement: The raw data supporting the conclusions of this article will be made available by the authors on request.

Conflicts of Interest: The authors declare no conflicts of interest.

References

1. Eberle, U.; Felderhoff, M.; Schüth, F. Chemical and physical solutions for hydrogen storage. *Angew. Chem. Int. Ed.* **2009**, *48*, 6608–6630. [CrossRef]
2. Muthukumar, P.; Kumar, A.; Afzal, M.; Bhogilla, S.; Sharma, P.; Parida, A.; Jana, S.; Kumar, E.A.; Pai, R.K.; Jain, I.P. Review on large-scale hydrogen storage systems for better sustainability. *Int. J. Hydrogen Energy* **2023**, *48*, 33223–33259. [CrossRef]
3. Shirizadeh, B.; Ailleret, A.; Guillon, A.; Bovari, E.; El Khatib, N.; Douguet, S.; Issa, C.B.; Brauer, J.; Trüby, J. Towards a resilient and cost-competitive clean hydrogen economy: The future is green. *Energy Environ. Sci.* **2023**, *16*, 6094–6109. [CrossRef]
4. Usman, M.R. Hydrogen storage methods: Review and current status. *Renew. Sustain. Energy Rev.* **2022**, *167*, 112743. [CrossRef]
5. Karayel, G.K.; Javani, N.; Dincer, I. A comprehensive assessment of energy storage options for green hydrogen. *Energy Convers. Manag.* **2023**, *291*, 117311. [CrossRef]
6. Ramsay, C.J.; Dinesh, K. High pressure direct injection of gaseous fuels using a discrete phase methodology for engine simulations. *Int. J. Hydrogen Energy* **2022**, *47*, 2017–2039. [CrossRef]
7. Al Ghafri, S.Z.S.; Munro, S.; Cardella, U.; Funke, T.; Notardonato, W.; Trusler, J.P.M.; Leachman, J.; Span, R.; Kamiya, S.; Pearce, G.; et al. Hydrogen liquefaction: A review of the fundamental physics, engineering practice and future opportunities. *Energy Environ. Sci.* **2022**, *15*, 2690–2731. [CrossRef]
8. Faye, O.; Szpunar, J.; Eduok, U. A critical review on the current technologies for the generation, storage, and transportation of hydrogen. *Int. J. Hydrogen Energy* **2022**, *47*, 13771–13802. [CrossRef]
9. Yartys, V.; Zhu, M. Recent advances in hydrogen storage materials. *J. Alloys Compd.* **2022**, *927*, 166892. [CrossRef]
10. Hassan, Q.; Sameen, A.Z.; Salman, H.M.; Jaszczur, M.; Al-Jiboory, A.K. Hydrogen energy future: Advancements in storage technologies and implications for sustainability. *J. Energy Storage* **2023**, *72*, 108404. [CrossRef]
11. Ye, J.H.; Jiang, L.J.; Li, Z.N.; Wang, S.M.; Wang, Q.; Luo, M.; Wu, Y.F.; Guo, X.M.; Wu, J.Q.; Zhang, L.Y. Optimization design of solid-state hydrogen storage device for fuel cell forklift. *J. Alloys Compd.* **2024**, *970*, 172242. [CrossRef]
12. Lototskyy, M.V.; Tarasov, B.P.; Yartys, V.A. Gas-phase applications of metal hydrides. *J. Energy Storage* **2023**, *72*, 108165. [CrossRef]
13. Tarasov, B.P.; Fursikov, P.V.; Volodin, A.A.; Bocharnikov, M.S.; Shimkus, Y.Y.; Kashin, A.M.; Yartys, V.A.; Chidziva, S.; Pasupathi, S.; Lototskyy, M.V. Metal hydride hydrogen storage and compression systems for energy storage technologies. *Int. J. Hydrogen Energy* **2021**, *46*, 13647–13657. [CrossRef]
14. Hardy, B.J.; Gamble, S.N. Material analysis of metal hydrides for bulk hydrogen storage. *Int. J. Hydrogen Energy* **2024**, *62*, 148–161. [CrossRef]
15. Zhang, X.Y.; Sun, Y.H.; Xia, G.L.; Yu, X.B. Light-weight solid-state hydrogen storage materials characterized by neutron scattering. *J. Alloys Compd.* **2022**, *899*, 163254. [CrossRef]
16. Lin, H.J.; Lu, Y.S.; Zhang, L.T.; Liu, H.Z.; Edalati, K.; Révész, A. Recent advances in metastable alloys for hydrogen storage: A review. *Rare Metals* **2022**, *41*, 1797–1817. [CrossRef]
17. Liu, H.; Zhang, J.X.; Sun, P.; Zhou, C.S.; Liu, Y.; Fang, Z.Z. An overview of TiFe alloys for hydrogen storage: Structure, processes, properties, and applications. *J. Energy Storage* **2023**, *68*, 107772. [CrossRef]
18. Sato, T.; Saitoh, H.; Utsumi, R.; Ito, J.; Nakahira, Y.; Obana, K.; Takagi, S.; Orimo, S.I. Hydrogen absorption reactions of hydrogen storage alloy $LaNi_5$ under high pressure. *Molecules* **2023**, *28*, 1256. [CrossRef]
19. Zhang, X.X.; Xiao, H.Q.; He, X.C.; Tang, R.Z.; Zhou, W.H.; Ma, C.M.; Hu, H.Z.; Chen, Q.J. Impacts of Y dopants on the microstructure and cyclic stability of TiCrVFeMo alloys. *Int. J. Hydrogen Energy* **2024**, *61*, 1220–1229. [CrossRef]
20. Zhu, Y.Y.; Li, X.B.; Yang, X.S.; Chen, P.Y.; Tsui, G.C.; Xu, Z.L.; Tang, R.H.; Xiao, F.M.; Chan, K.C. Compositionally complex doping for low-V Ti-Cr-V hydrogen storage alloys. *Chem. Eng. J.* **2023**, *477*, 146970. [CrossRef]

21. Wu, Y.F.; Zhao, W.; Jiang, L.J.; Li, Z.N.; Guo, X.M.; Ye, J.H.; Yuan, B.L.; Wang, S.M.; Hao, L. Effect of Fe and Al on hydrogen storage properties of 75 V-Ti-Cr alloys. *J. Alloys Compd.* **2021**, *887*, 161181. [CrossRef]
22. Xue, X.Y.; Ma, C.M.; Liu, Y.R.; Wang, H.; Chen, Q.J. Impacts of Ce dopants on the hydrogen storage performance of Ti-Cr-V alloys. *J. Alloys Compd.* **2023**, *934*, 167947. [CrossRef]
23. Singh, B.K.; Cho, S.W.; Bartwal, K.S. Microstructure and hydrogen storage properties of ($Ti_{0.32}Cr_{0.43}V_{0.25}$) + x wt%La(x = 0–10) alloys. *Int. J. Hydrogen Energy* **2014**, *39*, 8351–8356. [CrossRef]
24. Liu, X.P.; Jiang, L.J.; Li, Z.N.; Huang, Z.; Wang, S.M. Improve plateau property of Ti32Cr46V22 BCC alloy with heat treatment and Ce additive. *J. Alloys Compd.* **2009**, *471*, L36–L38. [CrossRef]
25. Lyu, J.Z.; Lider, A.; Kudiiarov, V. Using ball milling for modification of the hydrogenation/dehydrogenation process in magnesium-based hydrogen storage materials: An overview. *Metals* **2019**, *9*, 768. [CrossRef]
26. Yang, X.L.; Li, W.X.; Zhang, J.Q.; Hou, Q.H. Hydrogen storage performance of Mg/MgH_2 and its improvement measures: Research progress and trends. *Materials* **2023**, *16*, 1587. [CrossRef] [PubMed]
27. Li, Z.Y.; Sun, L.X.; Xu, F.; Luo, Y.M.; Xia, Y.P.; Wei, S.; Zhang, C.C.; Cheng, R.G.; Ye, C.F.; Liu, M.Y.; et al. Modulated noble metal/2D MOF heterostructures for improved hydrogen storage of MgH_2. *Rare Metals* **2023**, *43*, 1672–1685. [CrossRef]
28. Kwak, Y.J.; Song, M.Y.; Lee, K.T. Improvement in the hydrogen storage properties of MgH_2 by adding $NaAlH_4$. *Metals* **2024**, *14*, 227. [CrossRef]
29. Ding, Z.; Li, Y.T.; Yang, H.; Lu, Y.F.; Tan, J.; Li, J.B.; Li, Q.; Chen, Y.A.; Shaw, L.L.; Pan, F.S. Tailoring MgH_2 for hydrogen storage through nanoengineering and catalysis. *J. Magnes. Alloys* **2022**, *10*, 2946–2967. [CrossRef]
30. Yu, X.B.; Guo, Y.H.; Yang, H.; Wu, Z.; Grant, D.M.; Walker, G.S. Improved hydrogen storage in magnesium hydride catalyzed by nanosized $Ti_{0.4}Cr_{0.15}Mn_{0.15}V_{0.3}$ alloy. *J. Phys. Chem. C.* **2009**, *113*, 5324–5328. [CrossRef]
31. Lu, Z.Q.; Liu, H.Z.; Luo, H.; Wu, Z.Y.; Ning, H.; Fan, Y.; Wang, X.H.; Huang, X.T.; Huang, C.K.; Lan, Z.Q. Effect of $Ti_{0.9}Zr_{0.1}Mn_{1.5}V_{0.3}$ alloy catalyst on hydrogen storage kinetics and cycling stability of magnesium hydride. *Chem. Eng. J.* **2024**, *479*, 147893. [CrossRef]
32. Zhang, J.F.; Li, Z.N.; Wu, Y.F.; Guo, X.M.; Ye, J.H.; Yuan, B.L.; Wang, S.M.; Jiang, L.J. Synthesis, hydrogen storage properties and thermodynamic destabilization of Mg-$Ti_xCr_{0.8-x}V_{0.2}$ (x = 0.25, 0.35, 0.45, 0.55) nanocomposites. *J. Alloys Compd.* **2019**, *798*, 597–605. [CrossRef]
33. Yao, P.Y.; Ying, J.; Liu, Y.; Wu, C.Z.; Chou, K.C.; Lyu, T.; Li, Q. Catalytic effect of Ni@rGo on the hydrogen storage properties of MgH_2. *J. Magnes. Alloys* **2020**, *8*, 461–471. [CrossRef]
34. Pang, Y.P.; Li, Q. A review on kinetic models and corresponding analysis methods for hydrogen storage materials. *Int. J. Hydrogen Energy* **2016**, *41*, 18072–18087. [CrossRef]
35. *GB/T 33291-2016*; Measurement Method of Pressure-Composition-Temperature for Reversible Hydrogen Absorption & Desorption of Hydrides. National Standard of the People's Republic of China: Beijing, China, 2016.
36. Tamura, T.; Kazumi, T.; Kamegawa, A.; Takamura, H.; Okada, M. Protium absorption properties and protide formations of Ti-Cr-V alloys. *J. Alloys Compd.* **2003**, *356*, 505–509. [CrossRef]
37. Kumar, S.; Jain, A.; Ichikawa, T.; Kojima, Y.; Dey, G.K. Development of vanadium based hydrogen storage material: A review. *Renew. Sustain. Energy Rev.* **2017**, *72*, 791–800. [CrossRef]
38. Tamura, T.; Kazumi, T.; Kamegawa, A.; Takamura, H.; Okada, M. Effects of protide structures on hysteresis in Ti-Cr-V protium absorption alloys. *Mater. Trans.* **2002**, *43*, 2753–2756. [CrossRef]
39. Cao, Z.M.; Zhou, P.P.; Xiao, X.Z.; Zhang, H.K.; Jia, Y.X.; Zhan, L.J.; Piao, M.Y.; Li, Z.N.; Jiang, L.J.; Chen, L.X. Improved hydrogen ab-/desorption performance of Ti-Cr based alloys via dual-effect of oxide reduction and element substitution by minor Al additive. *Int. J. Hydrogen Energy* **2024**, *53*, 1123–1136. [CrossRef]
40. Zhang, J.F.; Li, Z.N.; Wu, Y.F.; Guo, X.M.; Ye, J.H.; Yuan, B.L.; Yuan, H.P.; Wang, S.M.; Jiang, L.J. Significant thermodynamic destabilization and superior hydrogen storage properties of nanocrystalline Mg-20 wt%Ti-Cr-V_x (x = 0.4, 0.6, 0.8; Ti/Cr = 2:3) composites synthesized by reactive ball milling. *J. Phys. Chem. C* **2019**, *123*, 15963–15976. [CrossRef]
41. Laversenne, L.; Andrieux, J.; Plante, D.; Lyard, L.; Miraglia, S. In operando study of TiVCr additive in MgH_2 composites. *Int. J. Hydrogen Energy* **2013**, *38*, 11937–11945. [CrossRef]
42. Chen, Y.; Li, Z.N.; Wu, Y.F.; Chen, W.; Yuan, H.P.; Hao, L.; Wang, S.H.; Wang, S.M. Synergetic effect of Ti_3C_2-X (X = Fe, Co, Ni) on enhanced hydrogen storage performance of MgH_2-TiCrV composite. *J. Alloys Compd.* **2024**, *976*, 173274. [CrossRef]
43. Chen, Y.P.; Sun, B.L.; Zhang, G.Q.; Wang, Y.Z.; Li, X.X. Catalytic effect of double transition metal sulfide $NiCo_2S_4$ on hydrogen storage properties of MgH_2. *Appl. Surf. Sci.* **2024**, *645*, 158801. [CrossRef]
44. Wang, M.X.; Wang, Y.G.; Kong, H.Y.; Xie, Q.F.; Wang, Y.; Chen, Y.G.; Yan, Y.G. Development of Fe-containing BCC hydrogen storage alloys with high vanadium concentration. *J. Alloys Compd.* **2023**, *958*, 170294. [CrossRef]
45. Hu, H.; Ma, C.; Chen, Q. Mechanism and microstructural evolution of TiCrVFe hydrogen storage alloys upon de-/hydrogenation. *J. Alloys Compd.* **2021**, *877*, 160315. [CrossRef]
46. Zhu, M.; Gao, Y.; Che, X.Z.; Yang, Y.Q.; Chung, C. Hydriding kinetics of nano-phase composite hydrogen storage alloys prepared by mechanical alloying of Mg and $MmNi_{5-x}(CoAlMn)_x$. *J. Alloys Compd.* **2002**, *330–332*, 708–713. [CrossRef]
47. Amirkhiz, B.S.; Zahiri, B.; Kalisvaart, P.; Mitlin, D. Synergy of elemental Fe and Ti promoting low temperature hydrogen sorption cycling of magnesium. *Int. J. Hydrogen Energy* **2011**, *36*, 6711–6722. [CrossRef]

48. Ren, C.; Fang, Z.Z.; Zhou, C.S.; Lu, J.; Ren, Y.; Zhang, X.Y. Hydrogen storage properties of magnesium hydride with V-based additives. *J. Phys. Chem. C* **2014**, *118*, 21778–21784. [CrossRef]
49. Li, Z.F.; Lu, Y.F.; Wang, J.F.; Chen, Y.A.; Li, Q.; Pan, F.S. Improved hydrogen storage kinetics of MgH_2 using $TiFe_{0.92}Mn_{0.04}Co_{0.04}$ with in-situ generated α-Fe as catalyst. *Mater. Rep. Energy* **2024**, *4*, 100247. [CrossRef]